Research Square

Preprints are preliminary reports that have not undergone peer review.
They should not be considered conclusive, used to inform clinical practice,
or referenced by the media as validated information.

Self-organized colloidal growth of stromatolites

Mei-Fu Zhou

zhoumeifu@mail.gyig.ac.cn

Department of Earth Sciences, the University of Hong Kong https://orcid.org/0009-0004-6617-7930

Wenhong Qiu

Institute of Geochemistry, Chinese Academy of Sciences https://orcid.org/0000-0002-0343-4010

Chris Ballhaus

University of Bonn

Article

Keywords:

Posted Date: November 4th, 2026

DOI: https://doi.org/10.21203/rs.3.rs-10972339/v1

License: This work is licensed under a Creative Commons Attribution 4.0 International License.
Read Full License

Additional Declarations: There is **NO** Competing Interest.

Title

Self-organized colloidal growth of stromatolites

Authors

Wenhong Johnson Qiu [1], Mei-Fu Zhou [1, 2, *], Chris Ballhaus [3, 1]

Affiliations

[1] *State Key Laboratory of Critical Mineral Research and Exploration, Institute of Geochemistry, Chinese Academy of Sciences, Guiyang 550081, China*

[2]*School of Earth Resource, China University of Geosciences (Wuhan), Wuhan 430074, China*

[3]*Institut Für Geowissenschaften, Universität Bonn, 53115, Bonn, Germany*

[*] Corresponding author, *E-mail: zhoumeifu@mail.gyig.ac.cn*

Abstract

Stromatolites have been widely regarded as key biosignatures of early life, yet the controls on their morphogenesis and diversity remain poorly constrained. Here, we investigate Mesoproterozoic ironstones from North China featuring stromatolitic structures and composed of laminated Fe(III)-oxyhydroxide colloids. Microstructural observations and colloidal stability calculations indicate that terrestrial colloids flocculated rapidly upon mixing with seawater in an estuarine environment and aggregated on the seafloor. We then numerically simulate the forming processes of stromatolites via diffusion-limited aggregation and surface diffusion (DLA–SD) mechanism and reveal that stromatolitic morphogenesis is primarily controlled by depositional and aggregation dynamics of colloids, which are related to geochemical and hydrodynamic conditions in estuaries. This DLA–SD framework also provides quantitative insights into the microbial sediment-trapping mechanisms for the formation of carbonate stromatolites and reveals that the diversification of morphologies of stromatolite were linked to the evolution of oceanic chemistry and microbial communities throughout the Earth history.

MAIN TEXT

1. Introduction

Stromatolites are laminated sedimentary structures that exhibit diverse morphologies, including domal, conical, columnar, and branching forms [1]. They are widely distributed within Precambrian shallow-marine carbonate platforms. The formation of carbonate stromatolites has been traditionally attributed to photosynthetic microbial mats, particularly cyanobacteria, which secrete extracellular polymeric substances (EPS). The EPS trap and bind carbonate particles, thereby promoting vertical accretion [2-4]. Consequently, morphologies of stromatolites have been widely used as proxies for the evolution of microbial ecosystems throughout the Earth's history [5-7].

The biogenic origin of stromatolites is studied mostly based on modern analogues in which microbial mats actively mediate carbonate precipitation and sediment stabilization [2,8-10]. However, the scarcity of unequivocal fossilized micro-organisms in Precambrian stromatolites has long fueled debate regarding their origin [11-13]. On the other hand, abiotic models, e.g., surface-normal growth, have been proposed to explain the formation of stromatolites, and numerical simulations and laboratory experiments have successfully reproduced some stromatolitic morphologies [13-15]. The central issue regarding this debate concerns the controls on diverse stromatolite morphogenesis and the extent to which biological activities play a role. Previous studies have proposed that the emergence, evolution and diversification of cyanobacteria drove the growth and morphological diversification of stromatolites [3]. In contrast, other models argue that organic matter functions only as a passive binding agent for sediment particles and does not directly regulate stromatolitic morphologies [14]. To resolve this controversy, two fundamental issues need to be addressed: (1) can stromatolitic morphogenesis arise through purely abiotic particle aggregation

and trapping processes? and (2) what roles do environmental parameters and organic matter play in initiating stromatolite growth and controlling the morphological diversity [1,14]?

Although stromatolites are predominantly composed of carbonates, there are stromatolitic and oolitic ironstones composed of laminated Fe(III)-oxyhydroxide colloidal aggregates [16-19]. Extensive studies have demonstrated that the dispersion stability of Fe(III)-oxyhydroxide colloids is highly sensitive to salinity and pH [20-23] and these colloids can undergo rapid flocculation and aggregation in response to shifts in these geochemical parameters [24-26].

Mesoproterozoic (ca. 1.7 Ga) ironstones are widely distributed in North China (Fig. 1), and display diverse stromatolitic morphologies (Fig. 2), closely resembling those of typical carbonate stromatolites [16,27]. Previous studies proposed that these Mesoproterozoic ironstones have negative δ^{56}Fe values (~−0.28‰), positive δ^{53}Cr values (~+1.56‰), negative εNd(t) values (~−6.3), elevated ^{187}Os/^{188}Os ratios (~0.6) and low ^{87}Sr/^{86}Sr ratios (~0.7063) indicative of derivation of Fe primarily from continental weathering of Fe-bearing volcanic rocks under relatively dynamic and oxygenated surface conditions after the Great Oxidation Event (GOE)–[28-31]. The tropical to subtropical paleolatitudes of the North China Craton at that time also favored this intense subaerial weathering [19,32]. These Fe(III)-oxyhydroxide particles were transported by rivers, flocculated and precipitated in a costal seawater settings with different pH and salinity. These stromatolitic ironstones therefore provide a unique opportunity to investigate whether stromatolitic morphogenesis can result from colloidal aggregation processes independent of microbial trapping, and to evaluate the environmental controls on the stromatolitic morphological diversity.

In this paper, we describe the sedimentary structures and micro- to nanoscale textures of stromatolitic ironstones from the Mesoproterozoic Chuanlinggou Formation in North China. The Derjaguin–Landau–Verwey–Overbeek (DLVO) theory is applied to model the dispersion stability

and aggregation behavior of Fe(III)-oxyhydroxide colloids under estuarine conditions. We further develop a process-based numerical model that integrates diffusion-limited aggregation and surface diffusion (DLA–SD) mechanisms to simulate the growth of stromatolites and reproduce their key morphological characteristics. Our results provide a new physicochemical framework for the formation of stromatolites, in addition to conventional biogenic models, and reveal a quantitative relationship between stromatolitic morphologies and environmental conditions.

2. Results

2.1 Geological background

The Mesoproterozoic Chuanlinggou Formation (~1.65 Ga) is extensively exposed across the Yanliao Basin within the North China Craton (NCC) (Figs. 1A and B). This formation unconformably overlies on the metamorphic basement and consist dominantly of quartz sandstones that grade laterally into limestones parallel to the paleo-shoreline (Fig. 1C). Stratigraphically, the sequence constitutes a classic transgressive succession, comprising basal sandstones intercalated with ironstone units, medial siltstones, and upper black shales (Figs. 1C, D). This transgressive architecture documents a depositional evolution from shallow, above wave-base tidal environments to deeper marine settings [16], reflecting the progressive subsidence of an epicontinental shelf developed within a carbonate platform associated with the breakup of the Columbia Supercontinent [33].

The ironstone layers exhibit exceptionally lateral persistence exceeding 150 km, grading southwestward into nearshore siliciclastic facies and northeastward into offshore mudstone facies (Figs. 1B and D). The associated sandstones preserve primary sedimentary structures, including cross-stratification, oscillation ripples, and mud cracks, diagnostic of a shallow intertidal to

subtidal shelf depositional regime [27]. Petrographically, the ironstones consist primarily of laminated hematite aggregates displaying both oolitic and stromatolitic fabrics (Fig. 2). Both the morphological expression and cumulative thickness of these ironstones display systematic spatial trends along paleo-environmental transects (Fig. 1) [16]. Specifically, oolitic ironstones form thin (<1 m) beds restricted to proximal, intertidal paleo-shoreline settings, e.g., that in the Majiayao section, whereas stromatolitic ironstones develop into thicker successions (up to 4 m) within distal, subtidal environments, e.g., that in the Laoyangou section (Figs.1B, D).

2.2 Petrography of stromatolitic ironstones

Stromatolitic ironstones in the Chuanlinggou formation have diverse morphologies, including domal, conical, columnar, and branching forms, with column diameters ranging from 5 to 25 mm and intercolumnar spaces of 1–5 mm filled by detrital quartz grains and silt-sized particles (Fig. 2). The stromatolitic bodies consist of alternating hematite laminae rich-in clay and depleted-in clay, respectively (~100 μm thick) (Figs. 3A–C). The lamination broadly conforms to stromatolite surfaces and display in most samples regular cyclic layering (~7.8–9.3 laminae mm^{-1}). These laminated structures indicate sustained upward accretion within a relatively low-energy coastal environment characterized by periodic fluctuations in sediment composition (Fig. 2).

Transmission electron microscopy (TEM) imaging reveals that the laminae are composed of aggregates of hematite together with subordinate illite nanocrystals (~100 nm in size; platy to needle-like morphologies) (Fig. 3). TEM observations further show that hematite laminae rich in clay minerals are characterized by loosely packed and randomly oriented hematite nanocrystals with dominant edge-to-face or edge-to-edge contacts, accompanied by illite- and SiO_2-filled pore spaces (Figs. 3D to F). In contrast, hematite laminae depleted in clay exhibit strongly aligned

hematite nanocrystals with dominant face-to-face contacts and only minor associated illite (Figs. 3G to I). These nanotextures suggest that the ironstones formed through particle aggregation rather than continuous crystal growth [34]. The systematic variations in mineral assemblages and particle orientations further imply that periodic fluctuations in water chemistry and hydrodynamic conditions controlled colloidal aggregation behavior within an estuarine environment [17,35].

2.3 Formation of ironstones via aggregation of hematite and illite nanoparticles

The stromatolitic ironstones are composed predominantly of hematite and subordinate clay (illite) nanoparticles within sizes of colloids (1 nm to 1 μm) [36]. Hematite particles are predominantly platy to needle-shaped in morphology, suggesting they are possibly pseudomorphs derived from the diagenetic dehydration of intermediate Fe(III)-oxyhydroxide precursors, such as acicular goethite (α-FeOOH) and/or platy lepidocrocite (γ-FeOOH) [37-39]. These precursors have a much lower energetic barrier for nucleation in water than hematite does [39]. The formation of stromatolitic ironstones was therefore likely governed by the aggregation behavior of Fe(III)-oxyhydroxide, a precursor to hematite, and clay colloids in an aqueous solution.

Clay minerals, such as illite, typically retain persistently negative surface charges across a wide pH range (~ 2.5 to 11) owing to permanent structural charges generated by isomorphous Al^{3+} substitution for Si^{4+} within the crystal lattice [40,41]. In contrast, Fe(III)-oxyhydroxide colloids acquire positive surface charges under acidic freshwater conditions through protonation of surface Fe–O and Fe–OH functional groups (e.g., $\equiv Fe–OH + H^+ \rightarrow \equiv Fe–OH_2^+$) and the development of electrostatic double layers (EDLs) surrounding the colloids (Fig. 4A). These positive surface charges stabilize colloidal dispersion in slightly acidic water through electrostatic repulsion [20,42-44]. Negatively charged clay colloids would therefore preferentially aggregate and bind with

positively charged Fe(III)-oxyhydroxide colloids through electrostatic attraction, providing a plausible explanation for the ubiquitous association of hematite and illite in the ironstones.

In addition, protonation of Fe(III)-oxyhydroxide colloids, particularly platy lepidocrocite (γ-FeOOH) nanocrystals, is both crystallographically anisotropic and highly sensitive to pH [20,21,43]. The (010) basal planes of lepidocrocite are dominated by relatively unreactive doubly-coordinated hydroxyl groups (≡Fe_2–OH) and are therefore only weakly protonated. By contrast, the (001) surfaces on the edges of lepidocrocite expose more reactive singly-coordinated hydroxyl groups (≡Fe–OH) and are readily protonated and positively charged [20]. Under acidic freshwater conditions, these anisotropically charged platy nanocrystals preferentially aggregate through edge-face contacts to minimize electrostatic repulsion between similarly charged crystal edges. Increasing pH progressively neutralizes the surface charges of Fe(III)-oxyhydroxide colloids, allowing platy particles to aggregate through face-to-face alignment driven predominantly by van der Waals attraction [20,42]. Consequently, the orientations of aggregation of Fe(III)-oxyhydroxide colloids were/are likely controlled by periodic fluctuations of water chemical environment in estuarine. During periods of enhanced discharge of mildly acidic clay-rich river water, FeOOH particles were preferentially aggregated through edge-to-face contacts to formFe(III)-oxyhydroxide laminae bearing clays. Conversely, with reduced freshwater input and relatively alkaline conditions, Fe(III)-oxyhydroxide colloids were aggregated through face-to-face alignment, leading to the formation of Fe(III)-oxyhydroxide laminae depleted in clays. In summary, the seasonal periodic changes of geochemical conditions in an estuarine environment triggers the variation in mineralogy and aggregation fabric of ironstones.

2.4 DLVO constraints on the stability of Fe(III)-oxyhydroxide colloids in estuarine settings

The transport and aggregation behavior of Fe(III)-oxyhydroxide colloids, which constitute the dominant mineral phase of the stromatolitic ironstones, were likely controlled by variations in colloidal dispersion stability in response to strong pH and salinity difference within estuarine environments [36,44,45]. The influence of pH and salinity on the stability of Fe(III)-oxyhydroxide colloids can be quantitatively evaluated using the DLVO theory [21,46]. That theory calculates the total interaction energy between colloids (V_{DLVO}) as the sum of attractive van der Waals interactions (V_{VDW}; negative energy) and repulsive electrostatic double-layer interactions (V_{EDL}; positive energy). Both are functions of pH and salinity (Fig. 4A) [22,36,46]. Details of the DLVO calculations are provided in the Methods section.

The DLVO calculations were performed across broad ranges of salinity (1–100% seawater) and pH (5–9). The results show that under slightly acidic (pH = 5) and low-salinity freshwater conditions (C_{NaCl} < 10 mM or < 2% seawater), a substantially positive energy barrier in V_{DLVO} develops (Fig. 4B). Under these conditions, decreasing the separation distance between colloids increases the total interaction energy ($V_{DLVO} > 0$), thereby inhibiting aggregation and stabilizing colloidal dispersions through electrostatic repulsion. However, increasing pH progressively neutralizes the surface charge of Fe(III)-oxyhydroxide colloids [21,36,38], and as pH approaches the point of zero charge (PZC; pH ≈ 8), the electrostatic repulsion energy (V_{EDL}) decreases substantially. This results in a collapse of the DLVO energy barrier (Fig. 4B). Consequently, colloids readily aggregate and flocculate to minimize the total interaction energy ($V_{DLVO} < 0$).

Similarly, increasing salinity (ionic strength) compresses the thickness of the electrostatic double layer surrounding Fe(III)-oxyhydroxide colloids (Eqs. 2 and 3), reducing the ζ zeta potential, which is the electric potential of the slipping plane of a colloidal particle, thereby

decreasing V_{EDL} [21,36] (Fig. 4C). Under near-neutral conditions (pH = 6), the DLVO energy barrier collapses at salinities of approximately 17–25% seawater, leading to rapid colloidal flocculation. These results therefore indicate that Fe(III)-oxyhydroxide colloids could remain stably dispersed within slightly acidic river water but would rapidly aggregate when river water mixes with seawater [21,36]. This interpretation is consistent with observations for flocculation of Fe(III)-oxyhydroxide colloids in modern estuaries [23,47] and with the hypothesis that ironstones were efficiently mineralized through estuarine colloidal flocculation processes [24-26,47].

To further investigate the growth mechanism of Fe(III)-oxyhydroxide colloidal aggregates following flocculation, additional DLVO calculations were performed for colloid–colloid and colloid–aggregate interactions. In these calculations, the colloidal aggregate was simplified as an infinitely extended platy collector (Fig. 4D; Eqs. 7–8 in Methods) [21,36,38]. The calculations reveal that the van der Waals interaction energy between a colloid and a larger-scale aggregate under high-pH and saline conditions is substantially lower than that between two individual colloids (Fig. 4D), indicating that suspended colloids are preferentially attached to existing aggregates on the seafloor rather than forming isolated particle pairs. Furthermore, V_{DLVO} decreases sharply only at very small separation distances (< 20 nm), suggesting that colloids can be captured efficiently only through the direct collision with aggregates driven by the Brownian motion and gravitational settling. These aggregation properties of Fe(III)-oxyhydroxide colloids provide a physicochemical basis for reconstructing the growth of stromatolitic ironstones, as demonstrated by the numerical simulations presented in the following sections.

2.5 Numerical simulation for the growth of stromatolitic ironstones via colloidal aggregation

The geochemical features and DLVO calculations indicate that stromatolitic ironstones were formed through the gravitational settling and aggregation of Fe(III)-oxyhydroxide colloids

in estuarine environments, where buoyant Fe(III)-oxyhydroxide-bearing river water was mixed with denser saline seawater wedges (Fig. 5A). However, the mechanisms governing stromatolitic growth and morphological diversification remain unresolved. To investigate these processes, we employed a process-based numerical approach that integrates diffusion-limited aggregation (DLA) [48,49] with surface diffusion (SD) mechanisms [50,51] to simulate the growth of stromatolites.

Diffusion-limited aggregation describes the clustering of nano-particles that undergo random motion, typically driven by the Brownian diffusion. It is commonly implemented via modelling random movement of particles within a two-dimensional lattice by a Monte Carlo method [48,49]. In the present model, DLA simulates the diffusive settling of small Fe(III)-oxyhydroxide colloidal clusters formed by flocculation in seawater and their subsequent attachment to pre-existing aggregates on the seafloor. Preferential downward settling of colloids is implemented by assigning a slightly higher probability of (1+pp)/(4+pp) for downward movement relative to the movement in the other three directions with probability of 1/(4+pp) (Figs. 5C and D). When the precipitation probability index is zero (pp = 0), colloidal motion becomes the isotropic Brownian movement, whereas increasing (pp) values produce progressively stronger vertical settling movements [51].

After the attachment of colloidal particles onto pre-existing aggregates, these particles are assumed not to become instantaneously fixed. Instead, they are allowed to diffuse along the aggregate surface within a finite surface diffusion radius (*sr*) to locate at energetically favorable positions with the highest number of neighboring contacts, thereby minimizing interfacial energy (Fig. 5E) [50-52]. The characteristic surface diffusion radius (*sr*) reflects the effective bonding strength between colloids and aggregates [51]. Stronger colloid–aggregate adhesion, resulting either

from enhanced chemical bonding or weaker hydrodynamic disturbance, produces smaller (*sr*) values, whereas weaker adhesion permits a longer-distance surface diffusion.

The simulations further incorporate the simultaneous Brownian motion of multiple colloids within the water column at a prescribed colloidal concentration (*cc*). Because natural colloidal suspensions are relatively diluted, colloids within the water column are scarcely clustered with one-another in water column, but will mostly precipitate to the seafloor and attach on the pre-existing aggregates directly [51]. Colloidal concentration was maintained dynamically by introducing a new colloid into the water column whenever an existing colloid became attached to the aggregate surface. To reproduce the periodic compositional layering observed in natural stromatolitic ironstones, the types of particles attached to aggregates (Fe(III)-oxyhydroxide versus clay) was periodically alternated and shown as different colors (Figs. 5C to E), simulating temporal variations in colloidal composition in estuarine environments.

A series of DLA–SD simulations were performed on a 200 × 128 two-dimensional lattice using a range of model parameters (*cc* = 0.02–0.06, *pp* = 0.1–1.7, and *sr* = 3–7). The simulation results are presented in Figures. 6–9 and movies. S1-S5. Details of the numerical implementation are provided in the Methods section.

3. Discussion

3.1 Growth mechanisms of stromatolites

The DLA–SD simulations successfully reproduce the major morphological features of stromatolites, including domal, conical, columnar, and branching structures, together with laminated textures conformable to depositional surfaces (Figs. 6–9). The simulations indicate that the growth of stromatolites proceeds through three successive stages: (1) Brownian motion and

gravitational settling of Fe(III)-oxyhydroxide colloids in the solution, (2) attachment of colloids to pre-existing aggregates on the substrate surface, and (3) subsequent surface diffusion of attached colloids toward nearby energetically favorable sites with the greatest number of neighboring contacts, thereby minimizing interfacial energy (Figs. 5 and 6, Movies. S1 to S5 in Supplementary files). Although the initial substrate surface is flat, domal morphologies emerge spontaneously and progressively evolve into more complex columnar and branching structures without requiring any external template or forcing mechanism (Movies. S1 to S5). Different stromatolitic structures, such as domal to branching were produced with change of simulation parameters of colloids.

This self-organized emergence of complex morphologies of stromatolites results from a positive feedback growth mechanism. Brownian motion and gravitational settling cause Fe(III)-oxyhydroxide colloids to be preferentially attached to aggregates with slightly elevated topography (Fig. 6). These elevated regions subsequently exhibit enhanced growth efficiency because they intercept and capture additional settling colloids more effectively, while simultaneously shadowing adjacent depressions from colloidal flux [49-52]. The interspace between columns in nature would be partially filled by detrital particles much later (Fig. 2). Over time, this dual positive-feedback process progressively amplifies minor topographic perturbations into distinct domal, columnar, and branching stromatolitic morphologies, in analogy to the growth of dendritic crystals [53].

Surface diffusion (SD), driven by relaxation of colloidal interfacial energy, is critical in the growth of stromatolites. Following initial attachment, colloids are able to migrate along aggregate surfaces toward nearby positions with the highest number of contacting neighbors (Fig. 5E) [5,51,54]. This SD process promotes structural compaction and stabilizes the columnar architecture of stromatolitic ironstones. In conventional DLA systems that lack surface diffusion, aggregates

typically develop highly fractal or dendritic morphologies [49,55], resembling the flocculated structures observed in laboratory Fe(III)-oxyhydroxide coagulation experiments and simulations [56,57]. In such experiments, high concentrations of Fe(III)-oxyhydroxide colloids rapidly coagulate upon mixing with saline water and therefore lack sufficient time for surface diffusion and interfacial energy relaxation [57]. In contrast, Fe(III)-oxyhydroxide colloid concentrations in natural estuarine environments were likely relatively low owing to limited supply of colloids and dilution by seawater. Under these conditions, colloids that settle onto aggregates retained sufficient time for surface diffusion, enabling particles to reorganize into energetically stable configurations with maximum interparticle contact, ultimately forming compact stromatolitic structures.

In summary, the DLA-SD simulations successfully reproduce the dynamic growth processes responsible for the diverse morphologies and laminated textures of stromatolitic ironstones. These results reveal that the coupled DLA–SD processes represent a plausible fundamental physical mechanism for stromatolite morphogenesis in estuarine settings.

3.2 Controls on the morphological diversity of stromatolites

To investigate the factors that control diverse morphologies of stromatolites, a series of variable-controlled simulations were conducted. The simulations successfully reproduce nearly the full spectrum of stromatolitic morphologies observed in natural ironstones (Figs. 7–9). The morphologies can be principally characterized by two geometric parameters: (1) intercolumnar spacing and (2) column diameter (Figs. 7–9). The modeling results demonstrate that intercolumnar spacing is controlled primarily by the precipitation probability index (*pp*) (Figs. 7 and 9). Diameters and overall structural compactness of columns is governed by the surface diffusion

radius (*sr*) (Figs. 8 and 9). In contrast, concentration of colloids (*cc*) exerts only a secondary, minor influence.

Increasing the precipitation probability index (*pp*) systematically decreases intercolumnar spacing and produces more densely packed stromatolitic structures (Figs. 7 and 9, Movies. S1 and S4). At low *pp* values, transport of colloids is dominated by the isotropic Brownian motion, allowing particles to diffuse laterally and preferentially attach to the flanks of existing columns and branches rather than settle into depressions to nucleate new columns (Figs. 7 and 9, Movie. S1). As *pp* increases, colloidal trajectories progressively transition toward vertically directed "ballistic" settling, increasing the probability that colloids reach topographic depressions hence initiating growth of closely spaced adjacent columns (Figs. 7 and 9, Movie. S4). In natural environments, Stoke's law predicts that the settling velocity increases as colloid sizes increase. Elevated Fe(III)-oxyhydroxide colloid concentrations or saturation states enhance nucleation-growth of colloids and collision frequency between colloids. Increases in pH promote colloidal aggregation. Both factors may promote smaller colloids to cluster onto larger ones, prior to entering the estuarine environment. Consequently, the aqueous geochemistry of river systems may indirectly influence stromatolitic morphology by regulating the size distribution and settling behavior of Fe(III)-oxyhydroxide colloids.

In contrast, decreasing the surface diffusion radius (sr) will reduce column diameter and progressively transform stromatolitic morphology from conical and domal forms into columnar and branching structures (Figs. 8 and 9, Movies. S1 and S5). This relationship arises from the interfacial energy minimization mechanism associated with surface diffusion. Continuous infilling of the marginal positions of colloidal aggregates with elevated topography promotes lateral expansion of stromatolitic columns until the characteristic width approaches the effective surface

diffusion radius. Consequently, larger (sr) values produce broader stromatolitic columns and more compact morphologies (Figs. 8 and 9, Movies. S5). When the *sr* values decrease and are sufficiently low, the distinct columnar and branching morphologies will result (Figs. 8–9, Movies. S1). Under low (sr) conditions, newly attached colloids can diffuse only short distances from their initial attachment sites, preserving the highly fractal growth geometry characteristic of conventional DLA systems lacking efficient surface diffusion [48,49]. Rather than contributing to lateral column thickening, colloids remain concentrated near protruding growth fronts, thereby promoting dendritic branching. The low (*pp*) values also can promote the development of dendritic structures, because decreasing *pp* values can enhance the probability that colloids migrate laterally and attach to the sides of existing columns, further stimulating branch formation (Figs. 8 and 9, Movies. S1).

As surface diffusion radius is inversely related to colloid–aggregate adhesion strength, variations in estuarine geochemical and hydrodynamic conditions likely exert strong controls on stromatolitic morphology. Lower salinity and lower pH reduce colloidal adhesion strength, whereas increased fluid turbulence can repeatedly detach recently deposited colloids from aggregate surfaces, thereby enhancing effective surface diffusion mobility. As a result, stromatolites formed in near-shore environments influenced by energetic hydrodynamic conditions and mildly acidic river-water input tend to develop coarser domal and thick-columnar morphologies. Heavy nearshore turbulence, however, often disrupts the steady settling of Fe(III)-oxyhydroxide aggregates on the seafloor, keeping them suspended and moving to ultimately stimulate ooid growth. Conversely, low-(*sr*) conditions may preferentially occur in more distal environments with elevated pH and salinities. In such a distal and low energetic zone, the precipitation index (*pp*) is also low because the hydrodynamic sorting during transport may

preferentially deliver finer colloidal particles. Therefore, the lower-energy and more saline distal environments favor narrower and more elongated columnar and branching structures.

The simulations further indicate that concentrations of colloids exert only limited influence on the morphology of stromatolites because we set the concentrations in our model to remain relatively low, thereby maintaining a DLA regime. At substantially higher colloidal concentrations, where precipitating colloids is no longer diffusion-limited, Fe(III)-oxyhydroxide particles would likely cluster together in water columns and precipitate rapidly and form laterally continuous laminae resembling banded iron formations. Our results therefore suggest that terrestrial Fe(III)-oxyhydroxide colloid concentrations in Mesoproterozoic estuarine systems were sufficiently elevated to maintain the growth of stromatolites but sufficiently diluted to preserve diffusion-limited aggregation behavior and generate the characteristic columnar-to-branching morphologies of stromatolites.

Overall, the DLA–SD simulations provide a robust, process-based approach capable of reproducing the complete morphological spectrum of stromatolites using only two parameters (*pp* and *sr*). This model establishes a direct genetic link between macroscopic stromatolitic morphology, ambient aqueous geochemistry, and local hydrodynamic conditions. Because these Mesoproterozoic stromatolitic ironstones in North China formed via the flocculation of terrestrial Fe(III)-oxyhydroxide colloids within estuarine settings, a process governed by a combination of global-scale atmospheric-oceanic conditions and localized estuarine dynamics, the systematic variations in their macro-morphology can serve as a sensitive archive of secular and spatial fluctuations in estuarine geochemistry and hydrodynamic energy.

3.3 Implications for the formation and evolution of stromatolites through earth history

3.3.1 The abiotic or biotic forming mechanism

The process-based DLA–SD model developed herein also has broader implications for understanding the morphogenesis of carbonate stromatolites sharing similar macroscopic structures [2,5,55,58]. Although this model is grounded in the physicochemical aggregation of Fe(III)-oxyhydroxide colloids, the underlying physical mechanism is not mineral-specific but reflects a general non-classical crystallization pathway driven by diffusion, aggregation, and surface-energy minimization. Recent studies have shown that calcium carbonate precipitates through the formation of stable prenucleation clusters and amorphous calcium carbonate (ACC) [59,60]. These stable clusters aggregate into ACC nanoparticles, which subsequently crystallize into carbonate minerals through particle-mediated pathways. Such non-classical crystallization provides a direct physical basis for extending the DLA–SD framework to carbonate stromatolites, where Brownian diffusion and aggregation of carbonate prenucleation clusters or ACC nanoparticles may similarly generate self-organized stromatolitic structures.

The precipitation probability (pp) reflects the probability that carbonate clusters diffuse in solutions and become irreversibly incorporated into the growing stromatolite. It is therefore governed by carbonate supersaturation, dissolved inorganic carbon and alkalinity of seawater [14,61]. Likewise, the surface diffusion radius (sr) represents the efficiency of local structural relaxation following particle attachment, driven by the minimization of interfacial free energy. Consequently, the stromatolitic structures can emerge naturally through a DLA-SD process without requiring biologically directed morphogenesis. Our simulations therefore suggest that at least some stromatolitic morphologies represent emergent physicochemical structures generated by universal self-organizing mineral aggregation.

However, this abiotic mechanism does not preclude biological influences. Instead, microorganisms likely regulate the physicochemical conditions under which particle-mediated mineralization operates. Microbial metabolism not only modifies seawater carbonate chemistry, pH, and alkalinity, thereby controlling carbonate supersaturation and the abundance of prenucleation clusters, it also enhances particle trapping and adhesion via bacterial EPS. For example, the properties of EPS like hydrophobicity and protein-to-carbohydrate [P/C] ratios would directly influence their adhesion strength [62]. In this context, microbial evolution primarily modulated the environmental conditions and particle-attachment efficiency, rather than fundamentally altering the underlying morphogenetic mechanism [1,14,61]. This unified framework reconciles the long-standing abiotic versus biotic debate by suggesting that stromatolite morphogenesis is fundamentally governed by universal self-organizing aggregation processes, while biology regulates the conditions under which these processes become effective.

3.3.2 The coupled evolution of stromatolite and paleoenvironment through earth history

Previous studies reveal that the morphologies of stromatolite evolved systematically through geological time (Fig. 10). Cuspate and conical forms dominated the Archean and reached their greatest abundance before the GOE, whereas branching and columnar morphologies became increasingly prevalent during the Mesoproterozoic and peaked in the Neoproterozoic (Fig. 10) [1,14,61]. Within the DLA–SD framework, these secular morphological transitions can be interpreted as consequences of long-term variations in the two fundamental morphogenetic parameters (*pp* and *sr*), which were jointly regulated by the co-evolution of ocean chemistry and microbial ecosystems.

Prior to the Great Oxidation Event (GOE), the high levels of atmospheric CO_2, combined with high oceanic Ca^{2+} concentration resulting from the elevated hydrothermal input and the

absence of CaCO3 accreting organisms, likely enhanced the alkalinity in ocean and maintained high carbonate saturation states [61,63,64]. These elevated saturation states promoted the rapid formation and aggregation of inorganic carbonate (aragonite) prenucleation clusters and ACC nanoparticles, corresponding to a high precipitation index (*pp*). Concurrently, relatively simple microbial communities probably produced EPS with comparatively weak particle-trapping efficiency [62,65], corresponding to a larger effective surface diffusion radius (*sr*). According to our simulations, this combination favors broad domal, cuspate, and conical stromatolites, matching the predominance of these morphologies in Archean successions (Figs. 9 and 10).

Following progressive Earth oxygenation of the Earth system during and after GOE, declining atmospheric CO_2 and reduced carbonate saturation decreased particle precipitation rates (lower *pp*). Although some studies suggest that ambient O_2 level during the mid-Proterozoic "Boring Billion" (1.8 to 0.8 Ga) were severely constrained (0.1 to 1% Present Atmospheric, PAL) [66], the deposition of the 1.65Ga Chuanlinggou ironstones indicates that the mid-Proterozoic surface seawater was largely free of dissolved iron ($Fe(II)_{aq}$) and substantially more oxidized than pre-GOE oceans, with oxygen levels pulsing up to ~ 4% PAL [67,68]. These transient atmospheric oxygenation pulses triggered the rapid evolution and diversification of microbial life, such as the emergency of eukaryotes [65,69]. This evolutionary advance likely enhanced EPS-mediated particle trapping and surface stickiness [62,65], effectively reducing the surface diffusion radius (lower *sr*). The DLA–SD model predicts that this parameter shift promotes increasingly columnar and branching stromatolites, matching their widespread expansion during the Mesoproterozoic and Neoproterozoic (Figs. 9 and 10) [61,65,69].

Importantly, the above interpretation does not require a change in the fundamental morphogenetic mechanism of stromatolites. Instead, stromatolite evolution can be viewed as the

response of a universal particle-mediated self-organizing system to long-term environmental forcing, with microbial evolution and secular changes in ocean chemistry acting primarily by modulating the governing parameters (*pp* and *sr*). Consequently, stromatolite morphologies not only record local hydrodynamic conditions but also the co-evolution of Earth's surface environments and the biosphere over geological time.

Methods

1. FIB–TEM analyses of minerals

Four TEM foils (~8 × 3 μm) were extracted from hematite-rich and clay-rich laminae in stromatolitic and oolitic ironstones using focused ion beam scanning electron microscopy (FIB) on an FEI Scios 2 HiVac instrument at the Shiyanjia Laboratory. The foils were mounted onto Cu TEM grids with support films and progressively thinned to ~50–100 nm using variable accelerating voltages and beam currents. Prior to analysis, the foils were stored in an anoxic glove box under N_2 atmosphere.

Transmission electron microscopy (TEM) analyses were conducted using an FEI Talos F200X G2 TEM operated at 200 kV at the laboratory of Shiyanjia Lab. Bright-field (BF) TEM imaging, selected-area electron diffraction (SAED), high-angle annular dark-field (HAADF) imaging, and energy-dispersive X-ray spectroscopy (EDS; detection limit ~1 wt%) were performed. HAADF imaging and EDS analyses were conducted in scanning a TEM (STEM) mode. Instrument calibration was carried out using diffraction ring patterns from a standard Au specimen. Elemental mapping was performed in STEM mode using the Oxford Aztec software.

2. DLVO calculation for colloidal stability

The kinetic stability and flocculation behavior of Fe(III) oxyhydroxide colloids in coastal environments can be quantitatively evaluated using Derjaguin–Landau–Verwey–Overbeek (DLVO) theory. This theory describes colloidal interaction energies as functions of solution ionic strength (salinity) and pH [21,22,36,46]. In the DLVO framework, Fe(III)-oxyhydroxide colloids are simplified as charged spherical nanoparticles surrounded by an electrical double layer (EDL) consisting of a compact Stern layer and an outer diffuse ion layer (Fig. 10B). The EDL generates electrostatic repulsive forces that counterbalance van der Waals attractive forces between particles, thereby controlling colloidal stability and aggregation behavior.

The total interaction energy between colloidal particles (V_{DLVO}) with similar radius (r) is expressed as the sum of van der Waals attraction (V_{VDM}) and electrostatic double-layer repulsion (V_{EDL}):

$$V_{DLVO}(s) = V_{VDW}(s) + V_{EDL}(s) \tag{1}$$

The electrostatic double-layer repulsion is calculated as:

$$V_{EDL}(s) = 2\pi\varepsilon_r\varepsilon_0 r\zeta^2\, ln(1 + e^{-ks}) \tag{2}$$

$$\kappa = \sqrt{\frac{1000e^2}{\varepsilon k_B T} S_I}, S_I = \sum_i z_i M_i \tag{3}$$

where ζ is the zeta potential that is the electrical potential at the slipping plane of a colloidal particle, $\varepsilon_r\varepsilon_0$ is the dielectric permittivity of the solution, k is the inverse Debye length (reciprocal

double-layer thickness), r is the particle radius and s is the separation distance between particle surfaces. The κ is controlled by ionic strength of solution (S_I) as shown in Eq. 3, where e is the elementary charge, k_B is the Boltzmann constant, T is temperature (in K), z_i is the valence and M_i is the concentration of ions i. The Eqs. 2 and 3 show that an increase in S_I will thus decrease the thickness of the double layer, reduce the electrostatic repulsion energy and facilitate colloidal aggregation. Additionally, ζ is controlled by pH of the solution. Experiments reveal that an increase in pH would reduces the protonation and surface charge of Fe(III)-oxyhydrogen colloids until approaching the point of zero charge (pH ~ 7.8 to 9.3 for goethite), which thus leads to a decrease in ζ and V_{EDL} (Table. S2) [21] and facilitate colloidal coalesce.

The van der Waals attractive potential between two colloids is expressed as:

$$V_{VDW}(s) = -\frac{A}{6}\left[\frac{2r^2}{s(4r+s)} + \frac{2r^2}{(2r+s)^2} + ln\frac{s(4r+s)}{(2r+s)^2}\right] \quad (4)$$

and can be simplified as

$$V_{VDW}(s) = -\frac{A}{12}\left[\frac{r}{s}\right] \quad (5)$$

where A is the Hamaker constant, which represents the intrinsic strength of long-range attractive interactions between colloidal particles [22]. The separation distance between particle surfaces is related to the center-to-center particle distance (a) according to:

$$s = a - 2r \tag{6}$$

In order evaluate the van der Waals attraction between a colloid and a large colloidal aggregate in a saline solution, in which V_{EDL} can be neglected, the surface of large aggregate is approximated as a large plate with infinite thickness. The van der Waals attractive potential between a colloid and a large plate is expresses as:

$$V_{VDW}(s) = -\frac{A}{6}[\frac{2r}{s} + \frac{2r}{s+4r} + ln\frac{s}{s+4r}] \tag{7}$$

and can be simplified to

$$V_{VDW}(s) = -\frac{A}{6}[\frac{r}{s}] \tag{8}$$

The Hamaker constant for Fe(III) oxyhydroxide systems has been experimentally constrained to approximately 2×10^{-20} J [70]. A particle radius of ~65 nm was adopted based on TEM observations. Previous experimental studies demonstrated that pH strongly influences protonation and deprotonation reactions on hematite surfaces, thereby controlling the ζ potential and electrostatic stability of Fe(III)-oxyhydroxide colloids [21]. The ζ potential and pH relations for Fe(III)-oxyhydroxide particle in 65 nm of He et al., 2008 [21] are adopted in this study. DLVO calculations indicate that both ionic strength (salinity) and pH exert major controls on the aggregation behavior of hematite colloids.

The kinetic dispersion stability of Fe(III)-oxyhydroxide colloids in estuarine environments can be modelled using DLVO theory [21,46]. This theory computes the total energy of interaction (V_{DLVO}) between colloids by the sum of energy contributions from the van der Waals attraction (V_{VDW}) and electrostatic double layer repulsion (V_{EDL}). Both are functions of distance (s) between particles in radius (r) (Eq. 1) [22,34,36,46].

$$V_{DLVO}(s) = V_{VDW}(s) + V_{EDL}(s) \tag{1}$$

$$V_{VDW}(s) = -\frac{A}{6}\left[\frac{2r^2}{s(4r+s)} + \frac{2r^2}{(2r+s)^2} + ln\frac{s(4r+s)}{(2r+s)^2}\right] \tag{2}$$

$$V_{EDL}(s) = 2\pi\varepsilon r\zeta^2\, ln(1 + e^{-\kappa s}) \tag{3}$$

$$\kappa = \sqrt{\frac{1000e^2}{\varepsilon k_B T}S_I}, S_I = \sum_i z_i M_i \tag{4}$$

The V_{VDW} term contributes the negative energy for V_{DLVO} (Fig. 10a) and can be calculated by Eq. 2, where A is the Hamaker constant, an intrinsic property of colloidal particles. The Hamaker constant represents the strength of long-range mutual attraction between two small particles [22], r is the particle radius, and s is the surface-surface distance between the particles. The V_{EDL} contributes the positive energy for V_{DLVO} (Fig. 10a) and can be calculated by Eq. 3, where ε is the dielectric permittivity of the solution, ζ the zeta potential of double layer, and κ the reciprocal double layer thickness. The κ is controlled by ionic strength of the solution (S_I) as shown by Eq. 4, where e is the elementary charge, k_B the Boltzmann constant, T (in K) the temperature,

z_i the valence, and M_i the concentration of ions i. The Eqs. 3 and 4 show that an increase in S_I will thus decrease the thickness of the double layer, reduce the electrostatic repulsion energy, hence facilitate colloidal aggregation. Additionally, ζ is controlled by the pH of the solution. Experiments reveal that an increase in pH would reduce the protonation and surface charge of Fe(III)-oxyhydrogen colloids until the point of zero charge (pH = 7.8 to 9.3 for goethite) is approached, leading to decreases in ζ and V_{EDL} [21] and facilitating colloidal coalesce.

3. Theory and implementation of DLA-SD simulation

Our numerical model is modified from the multiparticle biased DLA model with surface diffusion mechanism that was original proposed for the two-dimensional growth of electrodeposition [51]. Our simulation is based on the classic diffusion limited aggregation model and conducted in a two dimensional domain [48,49], in which Fe(III)-oxyhydroxide colloids, represented by mobilized voxels, can move randomly on the lattice until they attach to seeded aggregates and become immobilized. The simulate domain is defined on a two-dimensional lattice with horizontal and vertical grids of *Lx* and *Ly,* respectively. Periodic boundary conditions are applied in horizontal axis of lattice and reflective boundary condition is used at the top of lattice (Fig. 5C). The bottom of lattice is initialized as seeds of aggregates on the precipitation interface (Fig. 5C). The lattice is initialized by randomly distributing a number of random walkers (n) with assigned concentrations ($c=n/(Lx\times Ly)$). As simulation progresses, the random walkers keep Brownian movement, during which multiparticle movement biased each other can be regarded as a diffusion process (Fig. 5C). To model the slow, gravity-driven settling of Fe(III) colloids, the random moving colloids (a voxel in lattice) is programmed with a downward movement probability of $(pp+1)(pp+4)$ and a movement probability of $1/(pp+4)$ for the other three directions. Here, pp is a dimensionless precipitation probability index ranging from 0 to ∞ that represents the

settling velocity (Fig. 5D). Here, we choose relatively small *pp* values ranging from 0 to 2 to simulate the slow precipitation of Fe(III)-colloids in a quiet water column [51]. Based on the DLVO calculation for saline fluids, which shows a narrow Van der Waals radius (~10 nm) and stronger sphere-plate than sphere-sphere attraction, we assume that an Fe(III)-colloid will stick to the aggregates if it collides with or approaches them within a distance of less than 2 voxels. After attachment, a surface diffusion (SD) or relaxation mechanism of Fe(III)-colloids on active surface of aggregates [5,50,51] will set in (Fig. 5E). If an Fe (III)-colloid sticks to an aggregate, it can diffuse immediately along an aggregate surface within a certain diffusion radius (*sr*) to find the most stable position, where aggregate contact is maximized to yield the strongest attractive force, while displacement is minimized to ensure peak energy efficiency. The diffusion radius (sr) represents the relaxation capacity of colloids on the active surface within a characteristic timeframe [5,51]. To simulate an infinitely high system where the distance between colloids greatly exceeds their lateral dimensions, the mean colloidal concentration (cc) is kept constant; as particles attach to the aggregate, new ones are generated at the top of the lattice. This setup ensures a constant particle flux throughout all stages of the simulation.

During the simulation, an unattached active colloid is randomly selected to undergo Brownian motion (random movement through space). If this colloid successfully attaches to the aggregate, surface diffusion modeling is performed for it. If it fails to attach, the round ends, and a new active colloid is selected. For a system starting with n active colloids in solution, a single time step is defined as n interactions, ensuring that every active colloid is approximately iterated.

Additionally, to simulate the shifting composition of precipitates (such as Fe(III)-oxyhydroxide or clay) in an estuarine environment, the type—and corresponding color—of the

particles attaching to the aggregate is changed periodically. This cycling period is determined by the number of particles (n) required to accumulate a laminate of a specific thickness.

References

1 Bosak, T., Knoll, A. H. & Petroff, A. P. The Meaning of Stromatolites. *Annu. Rev. Earth Planet. Sci.* **41**, 21-44, doi:10.1146/annurev-earth-042711-105327 (2013).

2 Noffke, N. & Awramik, S. Stromatolites and MISS—differences between relatives. *Gsa Today* **23** (2013).

3 Dupraz, C. *et al.* Processes of carbonate precipitation in modern microbial mats. *Earth-Sci. Rev.* **96**, 141-162, doi:https://doi.org/10.1016/j.earscirev.2008.10.005 (2009).

4 Riding, R. in *Advances in Stromatolite Geobiology* (eds Joachim Reitner, Nadia-Valérie Quéric, & Gernot Arp) 29-74 (Springer Berlin Heidelberg, 2011).

5 Dupraz, C., Pattisina, R. & Verrecchia, E. P. Translation of energy into morphology: Simulation of stromatolite morphospace using a stochastic model. *Sedimentary Geology* **185**, 185-203, doi:https://doi.org/10.1016/j.sedgeo.2005.12.012 (2006).

6 Hohl, S. V. & Viehmann, S. Stromatolites as geochemical archives to reconstruct microbial habitats through deep time: Potential and pitfalls of novel radiogenic and stable isotope systems. *Earth-Sci. Rev.* **218**, 103683, doi:https://doi.org/10.1016/j.earscirev.2021.103683 (2021).

7 Webb, G. E. & Kamber, B. S. in *Earliest Life on Earth: Habitats, Environments and Methods of Detection* (eds Suzanne D. Golding & Miryam Glikson) 127-170 (Springer Netherlands, 2011).

8 Freytet, P. & Verrecchia, E. P. Freshwater organisms that build stromatolites: a synopsis of biocrystallization by prokaryotic and eukaryotic algae. *Sedimentology* **45**, 535-563 (1998).

9 Bebout, B. *et al.* Long-Term Manipulations of Intact Microbial Mat Communities in a Greenhouse Collaboratory: Simulating Earth's Present and Past Field Environments. *Astrobiology* **2**, 383-402, doi:10.1089/153110702762470491 (2002).

10 Reid, R. P. *et al.* The role of microbes in accretion, lamination and early lithification of modern marine stromatolites. *Nature* **406**, 989-992, doi:10.1038/35023158 (2000).

11 Buick, R. The Antiquity of Oxygenic Photosynthesis: Evidence from Stromatolites in Sulphate-Deficient Archaean Lakes. *Science* **255**, 74-77, doi:10.1126/science.11536492 (1992).

12 Brasier, M., McLoughlin, N., Green, O. & Wacey, D. A fresh look at the fossil evidence for early Archaean cellular life. *Philos Trans R Soc Lond B Biol Sci* **361**, 887-902, doi:10.1098/rstb.2006.1835 (2006).

13 Grotzinger, J. P. & Rothman, D. H. An abiotic model for stromatolite morphogenesis. *Nature* **383**, 423-425, doi:10.1038/383423a0 (1996).

14 Grotzinger, J. P. & Knoll, A. H. Stromatolites in Precambrian carbonates: Evolutionary Mileposts or Environmental Dipsticks? *Annu. Rev. Earth Planet. Sci.* **27**, 313-358, doi:https://doi.org/10.1146/annurev.earth.27.1.313 (1999).

15 McLoughlin, N., Wilson, L. A. & Brasier, M. D. Growth of synthetic stromatolites and wrinkle structures in the absence of microbes – implications for the early fossil record. *Geobiology* **6**, 95-105, doi:https://doi.org/10.1111/j.1472-4669.2007.00141.x (2008).
16 Lin, Y., Tang, D., Shi, X., Zhou, X. & Huang, K. Shallow-marine ironstones formed by microaerophilic iron-oxidizing bacteria in terminal Paleoproterozoic. *Gondwana Research* **76**, 1-18, doi:https://doi.org/10.1016/j.gr.2019.06.004 (2019).
17 Caraballo, M. A., Sarmiento, A. M., Sánchez-Rodas, D., Nieto, J. M. & Parviainen, A. Seasonal variations in the formation of Al and Si rich Fe-stromatolites in the highly polluted acid mine drainage of Agua Agria Creek (Tharsis, SW Spain). *Chem. Geol.* **284**, 97-104, doi:https://doi.org/10.1016/j.chemgeo.2011.02.012 (2011).
18 Salama, W., El Aref, M. & Gaupp, R. Mineral evolution and processes of ferruginous microbialite accretion -an example from the Middle Eocene stromatolitic and ooidal ironstones of the Bahariya Depression, Western Desert, Egypt. *Geobiology* **11**, 15-28 (2013).
19 Lechte, M. *et al.* Oolitic ironstones, continental iron flux and reverse weathering in the Proterozoic Eon: Insights from the Tonian Katherine Group, Yukon. *Earth-Sci. Rev.* **253**, 104790, doi:https://doi.org/10.1016/j.earscirev.2024.104790 (2024).
20 Kozin, P. A., Salazar-Alvarez, G. & Boily, J.-F. Oriented Aggregation of Lepidocrocite and Impact on Surface Charge Development. *Langmuir* **30**, 9017-9021, doi:10.1021/la500507e (2014).
21 He, Y. T., Wan, J. & Tokunaga, T. Kinetic stability of hematite nanoparticles: the effect of particle sizes. *Journal of Nanoparticle Research* **10**, 321-332, doi:10.1007/s11051-007-9255-1 (2008).
22 Plaza, R. C., Quirantes, A. & Delgado, A. V. Stability of Dispersions of Colloidal Hematite/Yttrium Oxide Core-Shell Particles. *Journal of Colloid and Interface Science* **252**, 102-108, doi:https://doi.org/10.1006/jcis.2002.8459 (2002).
23 Hunter, K. A., Leonard, M. R., Carpenter, P. D. & David Smith, J. Aggregation of iron colloids in estuaries: a heterogeneous kinetics study using continuous mixing of river and sea waters. *Colloids and Surfaces A: Physicochemical and Engineering Aspects* **120**, 111-121, doi:https://doi.org/10.1016/S0927-7757(96)03719-3 (1997).
24 Raiswell, R. Iron Transport from the Continents to the Open Ocean: The Aging–Rejuvenation Cycle. *Elements* **7**, 101-106, doi:10.2113/gselements.7.2.101 (2011).
25 Pufahl, P. K., Pirajno, F. & Hiatt, E. E. Riverine mixing and fluvial iron formation: A new type of Precambrian biochemical sediment. *Geology* **41**, 1235-1238, doi:10.1130/G34812.1 (2013).
26 Novoselov, K. A., Belogub, E. V., Kotlyarov, V. A., Filippova, K. A. & Sadykov, S. A. Mineralogical and Geochemical Features of Oolitic Ironstones from the Sinara–Techa Deposit, Kurgan District, Russia. *Geology of Ore Deposits* **60**, 265-276, doi:10.1134/S1075701518030066 (2018).
27 Tang, D., Xie, B., Shi, X. & Zhou, X. Low level of phosphorous concentration in terminal Paleoproterozoic shallow seawater: Evidence from Chuanlinggou ironstone on North China Platform. *Precambrian Research* **370**, 106554, doi:https://doi.org/10.1016/j.precamres.2021.106554 (2022).
28 Li, Z. & Zhu, X. Geochemical features of Xuanlong type iron ore deposit in Hebei Province and their geological significance. *Acta Petrologica Sinica* **28**, 2903-2911 (2012).

29 Chu, Z. *et al.* Re-Os, Sr-Nd isotopic and PGE elemental constraints for the formation of mid-Proterozoic ironstones in North China Craton: Implications for the atmospheric oxygen level. *Earth Planet. Sci. Lett.* **621**, 118367, doi:https://doi.org/10.1016/j.epsl.2023.118367 (2023).
30 Qiu, Y., Qin, L., Huang, F., Zhao, T. & Li, Y. Early Prosperity of Iron Bacteria at the End of the Paleoproterozoic Era. *Geophysical Research Letters* **49**, e2022GL097877, doi:https://doi.org/10.1029/2022GL097877 (2022).
31 Liu, S., Jia, C., Zhu, X., Su, W. & Zhao, T. Mo-isotope constraints on the mid-Proterozoic ocean oxidation: Insights from the black shales of the∼ 1.64 Ga Chuanlinggou Formation, North China Craton. *Palaeogeography, Palaeoclimatology, Palaeoecology* **675**, 113077 (2025).
32 Cai, Y. *et al.* Paleomagnetic constraints on the primary iron minerals of the late Paleoproterozoic Xuanlong-type ironstone in the North China Craton. *Earth Planet. Sci. Lett.* **647**, 119013, doi:https://doi.org/10.1016/j.epsl.2024.119013 (2024).
33 Duan, C. *et al.* U-Pb Ages and Hf Isotopes of Detrital Zircon Grains from the Mesoproterozoic Chuanlinggou Formation in North China Craton: Implications for the Geochronology of Sedimentary Iron Deposits and Crustal Evolution. *Minerals* **8** (2018).
34 De Yoreo, J. J. *et al.* Crystallization by particle attachment in synthetic, biogenic, and geologic environments. *Science* **349**, aaa6760, doi:10.1126/science.aaa6760 (2015).
35 Nichols, M. M. Sediment accumulation rates and relative sea-level rise in lagoons. *Marine Geology* **88**, 201-219, doi:https://doi.org/10.1016/0025-3227(89)90098-4 (1989).
36 Guo, Y. *et al.* The aggregation of natural inorganic colloids in aqueous environment: A review. *Chemosphere* **310**, 136805, doi:https://doi.org/10.1016/j.chemosphere.2022.136805 (2023).
37 Putnis, A. Mineral Replacement Reactions. *Reviews in Mineralogy and Geochemistry* **70**, 87-124, doi:10.2138/rmg.2009.70.3 (2009).
38 Walsch, J. & Dultz, S. Effects of pH, Ca- and SO4-concentration on surface charge and colloidal stability of goethite and hematite – consequences for the adsorption of anionic organic substances. *Clay Minerals* **45**, 1-13, doi:10.1180/claymin.2010.045.1.01 (2010).
39 Weibel, R. & Grobety, B. Pseudomorphous transformation of goethite needles into hematite in sediments of the Triassic Skagerrak Formation, Denmark. *Clay Minerals* **34**, 657-660 (1999).
40 Kriaa, A., Hamdi, N. & Srasra, E. Proton adsorption and acid-base properties of Tunisian illites in aqueous solution. *Journal of Structural Chemistry* **50**, 273-287, doi:10.1007/s10947-009-0039-6 (2009).
41 Forbes, E. & Chryss, A. in *Clays in the Minerals Processing Value Chain* (eds Markus Gräfe, Craig Klauber, Angus J. McFarlane, & David J. Robinson) 81-110 (Cambridge University Press, 2017).
42 Boily, J.-F. & Kozin, P. A. Particle morphological and roughness controls on mineral surface charge development. *Geochimica et Cosmochimica Acta* **141**, 567-578, doi:https://doi.org/10.1016/j.gca.2014.06.016 (2014).
43 Rustad, J. R., Wasserman, E. & Felmy, A. R. Molecular modeling of the surface charging of hematite: II. Optimal proton distribution and simulation of surface charge versus pH relationships. *Surface Science* **424**, 28-35, doi:https://doi.org/10.1016/S0039-6028(99)00009-6 (1999).

44 Ohtsubo, M., Yoshimura, A., Wada, S.-I. & Yong, R. N. Particle Interaction and Rheology of Illite-Iron Oxide Complexes. *Clays and Clay Minerals* **39**, 347-354, doi:10.1346/CCMN.1991.0390402 (1991).
45 Kim, S., Lee, K.-S., Zachariah, M. R. & Lee, D. Three-dimensional off-lattice Monte Carlo simulations on a direct relation between experimental process parameters and fractal dimension of colloidal aggregates. *Journal of Colloid and Interface Science* **344**, 353-361, doi:https://doi.org/10.1016/j.jcis.2010.01.008 (2010).
46 Hotze, E. M., Phenrat, T. & Lowry, G. V. Nanoparticle Aggregation: Challenges to Understanding Transport and Reactivity in the Environment. *Journal of Environmental Quality* **39**, 1909-1924, doi:https://doi.org/10.2134/jeq2009.0462 (2010).
47 Boyle, E., Edmond, J. & Sholkovitz, E. The mechanism of iron removal in estuaries. *Geochimica et Cosmochimica Acta* **41**, 1313-1324 (1977).
48 Meakin, P. Diffusion-controlled cluster formation in two, three, and four dimensions. *Physical Review A* **27**, 604-607, doi:10.1103/PhysRevA.27.604 (1983).
49 Witten, T. A. & Sander, L. M. Diffusion-Limited Aggregation, a Kinetic Critical Phenomenon. *Physical Review Letters* **47**, 1400-1403, doi:10.1103/PhysRevLett.47.1400 (1981).
50 García-Ruiz, J. M. & Otálora, F. Diffusion limited aggregation. The role of surface diffusion. *Physica A: Statistical Mechanics and its Applications* **178**, 415-420, doi:https://doi.org/10.1016/0378-4371(91)90030-G (1991).
51 Castro, M., Cuerno, R., Sánchez, A. & Domínguez-Adame, F. Multiparticle biased diffusion-limited aggregation with surface diffusion: A comprehensive model of electrodeposition. *Physical Review E* **62**, 161-173, doi:10.1103/PhysRevE.62.161 (2000).
52 Duarte-Neto, P., Stošić, T., Stošić, B., Lessa, R. & Milošević, M. V. Interplay of model ingredients affecting aggregate shape plasticity in diffusion-limited aggregation. *Physical Review E* **90**, 012312, doi:10.1103/PhysRevE.90.012312 (2014).
53 Meakin, P. The growth of rough surfaces and interfaces. *Physics Reports* **235**, 189-289, doi:https://doi.org/10.1016/0370-1573(93)90047-H (1993).
54 Vishnugopi, B. S., Hao, F., Verma, A. & Mukherjee, P. P. Surface diffusion manifestation in electrodeposition of metal anodes. *Physical Chemistry Chemical Physics* **22**, 11286-11295, doi:10.1039/D0CP01352H (2020).
55 Verrecchia, E. Morphometry of microstromatolites in calcrete laminar crusts and a fractal model of their growth. *Mathematical Geology* **28**, 87-109, doi:10.1007/BF02273525 (1996).
56 Xiong, Y., Liu, X. & Xiong, H. Aggregation modeling of the influence of pH on the aggregation of variably charged nanoparticles. *Scientific Reports* **11**, 17386, doi:10.1038/s41598-021-96798-3 (2021).
57 Destefani, T. A., Lavansdoski Onaga, G., de Farias, M. A., Percebom, A. M. & Sabadini, E. Stabilization of spherical nanoparticles of iron(III) hydroxides in aqueous solution by wormlike micelles. *Journal of Colloid and Interface Science* **513**, 527-535, doi:https://doi.org/10.1016/j.jcis.2017.11.035 (2018).
58 Pamela Reid, R., James, N. P., Macintyre, I. G., Dupraz, C. P. & Burne, R. V. Shark Bay stromatolites: Microfabrics and reinterpretation of origins. *Facies* **49**, 299-324, doi:10.1007/s10347-003-0036-8 (2003).
59 Gebauer, D. & Cölfen, H. Prenucleation clusters and non-classical nucleation. *Nano Today* **6**, 564-584, doi:https://doi.org/10.1016/j.nantod.2011.10.005 (2011).

60 Gebauer, D., Völkel, A. & Cölfen, H. Stable Prenucleation Calcium Carbonate Clusters. *Science* **322**, 1819-1822, doi:10.1126/science.1164271 (2008).
61 Cantine, M. D., Knoll, A. H. & Bergmann, K. D. Carbonates before skeletons: A database approach. *Earth-Sci. Rev.* **201**, 103065, doi:https://doi.org/10.1016/j.earscirev.2019.103065 (2020).
62 Chen, C.-S. *et al.* Stickiness of extracellular polymeric substances on different surfaces via magnetic tweezers. *Science of The Total Environment* **757**, 143766, doi:https://doi.org/10.1016/j.scitotenv.2020.143766 (2021).
63 Grotzinger John, P. & Kasting James, F. New Constraints on Precambrian Ocean Composition. *The Journal of Geology* **101**, 235-243, doi:10.1086/648218 (1993).
64 Kempe, S. & Degens, E. T. An early soda ocean? *Chem. Geol.* **53**, 95-108, doi:https://doi.org/10.1016/0009-2541(85)90023-3 (1985).
65 Awramik, S. M. & Riding, R. Role of algal eukaryotes in subtidal columnar stromatolite formation. *Proceedings of the National Academy of Sciences* **85**, 1327-1329, doi:10.1073/pnas.85.5.1327 (1988).
66 Planavsky, N. J. *et al.* Low Mid-Proterozoic atmospheric oxygen levels and the delayed rise of animals. *Science* **346**, 635-638, doi:10.1126/science.1258410 (2014).
67 Zhang, S., Wang, H., Wang, X. & Ye, Y. The Mesoproterozoic Oxygenation Event. *Science China Earth Sciences* **64**, 2043−2068 (2022).
68 Hardisty, D. S. *et al.* Perspectives on Proterozoic surface ocean redox from iodine contents in ancient and recent carbonate. *Earth Planet. Sci. Lett.* **463**, 159-170, doi:https://doi.org/10.1016/j.epsl.2017.01.032 (2017).
69 Huang, J. *et al.* The oxygen cycle and a habitable Earth. *Science China Earth Sciences* **64**, 511-528, doi:10.1007/s11430-020-9747-1 (2021).
70 Schudel, M., Behrens, S. H., Holthoff, H., Kretzschmar, R. & Borkovec, M. Absolute Aggregation Rate Constants of Hematite Particles in Aqueous Suspensions: A Comparison of Two Different Surface Morphologies. *Journal of Colloid and Interface Science* **196**, 241-253, doi:https://doi.org/10.1006/jcis.1997.5207 (1997).

Acknowledgments

We than Prof. Zerui Liu for his help with sampling, Prof. Tai-Ping Zhao and Prof. Ying Cui for their valuable discussions for the project. The study was funded by the National Natural Science Foundation of China (Grant No. 42302095) granted to WHJQ and financially supported by the Institute of Geochemistry, Chinese Academy of Sciences and China University of Geosciences (Wuhan) to MFZ.

Author contributions:

Investigation: WHJQ, MFZ, CB

Methodology, Conceptualization, Codes and Visualization: WHJQ

Supervision: MFZ

Writing—original draft: WHJQ

Writing—review & editing: MFZ, CB, WHJQ

Competing interests: Authors declare that they have no competing interests.

Data and materials availability: The data, code that support this paper are available from the corresponding author (MFZ) and the first author (WHJQ) upon reasonable request.

Figures

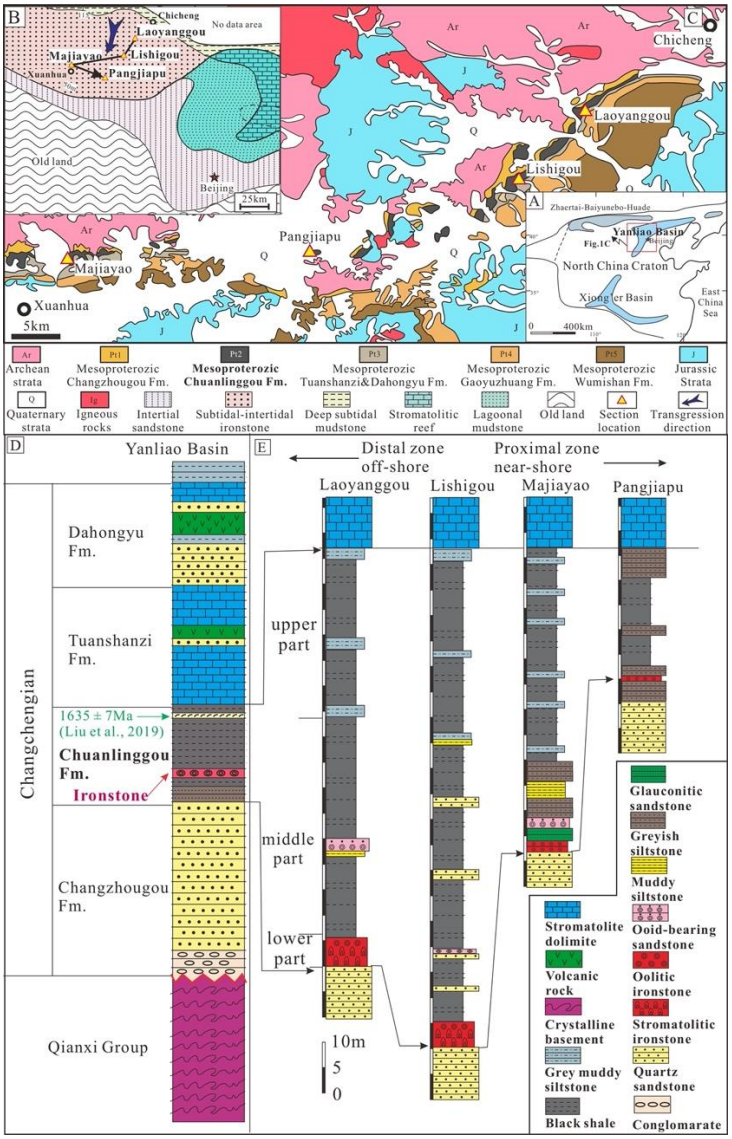


Fig. 1 Geological setting and stratigraphy of the late Paleoproterozoic–early Mesoproterozoic Chuanlinggou, North China Craton. (A) Distribution of the Yanliao basins in the North China Craton during early Mesoproterozoic. (B) Paleogeographic reconstruction of the Yanliao Basin during deposition of the Chuanlinggou Formation. (C) Simplified geological map of the study area. (D) Stratigraphic columns of the Changcheng System in the Yanliao regions. (E) Stratigraphic correlation of the Chuanlinggou Formation among different sections shown in Fig. 1B. Maps and stratigraphy are modified after Tang et al., 2022.

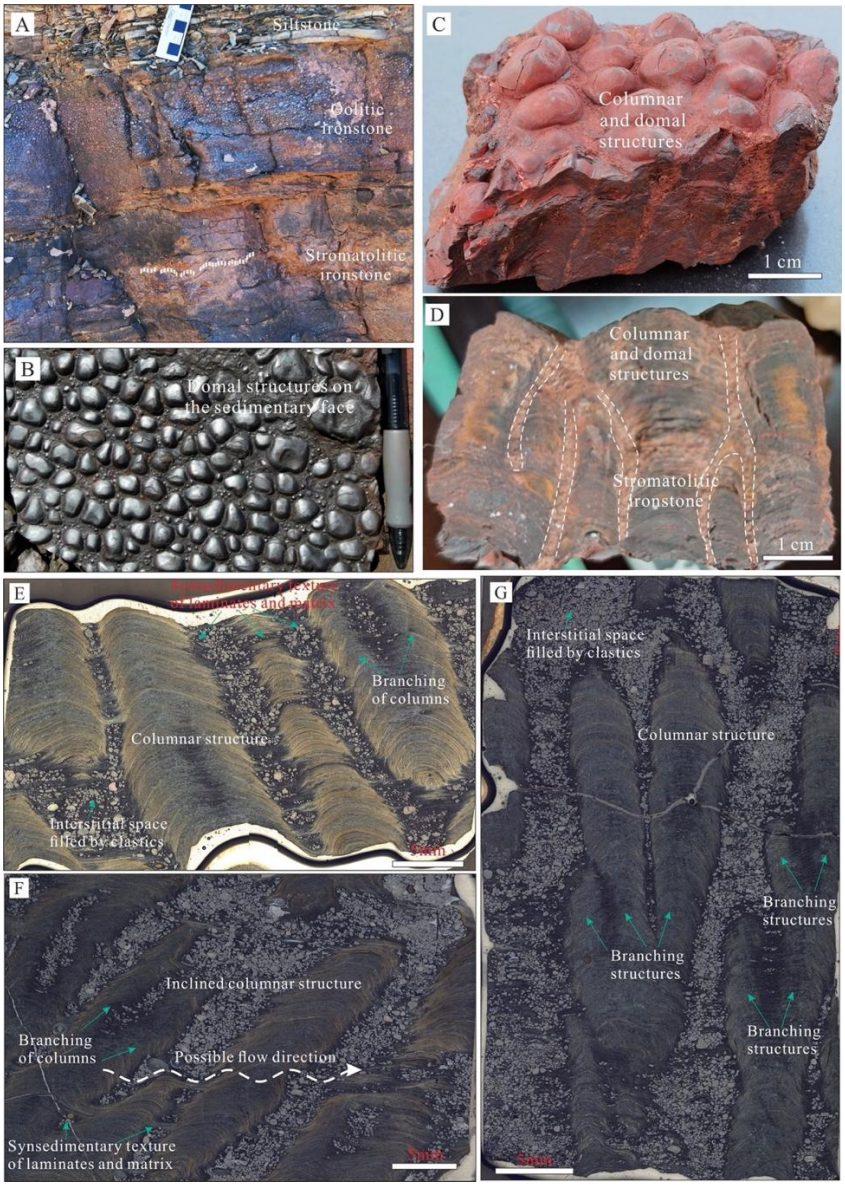


Fig. 2 Field outcrops, hand specimens of microscopy pictures of ironstones. (A) Outcrop showing lithological successions of the Chuanlinggou Formation, including transitional layers of oolitic ironstone, stromatolitic ironstone, and sandstone. (B) Domal structures of stromatolitic ironstone on sedimentary face. (C) and (D) Hand specimen of stromatolitic ironstone showing columnar structures. (E) to (G) Photographs of polished stromatolitic ironstone sections showing variable columnar and branching morphologies and internal laminated textures.

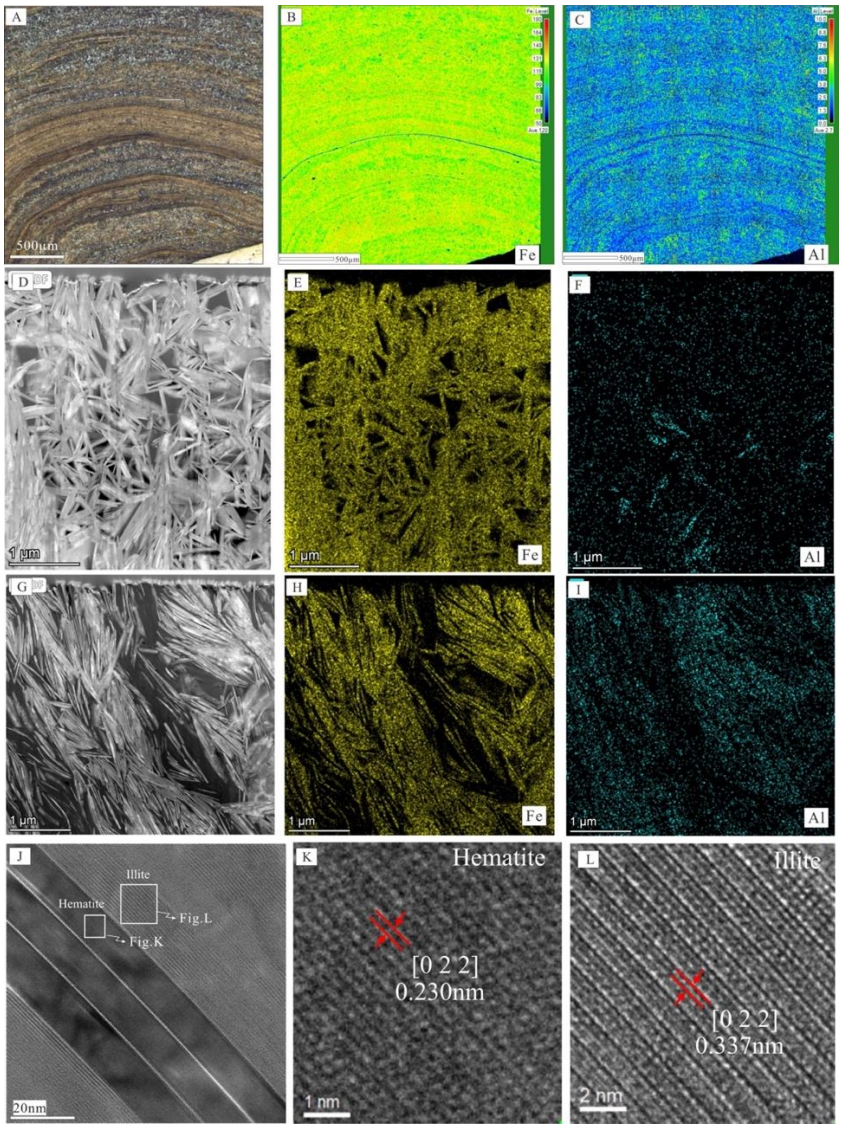
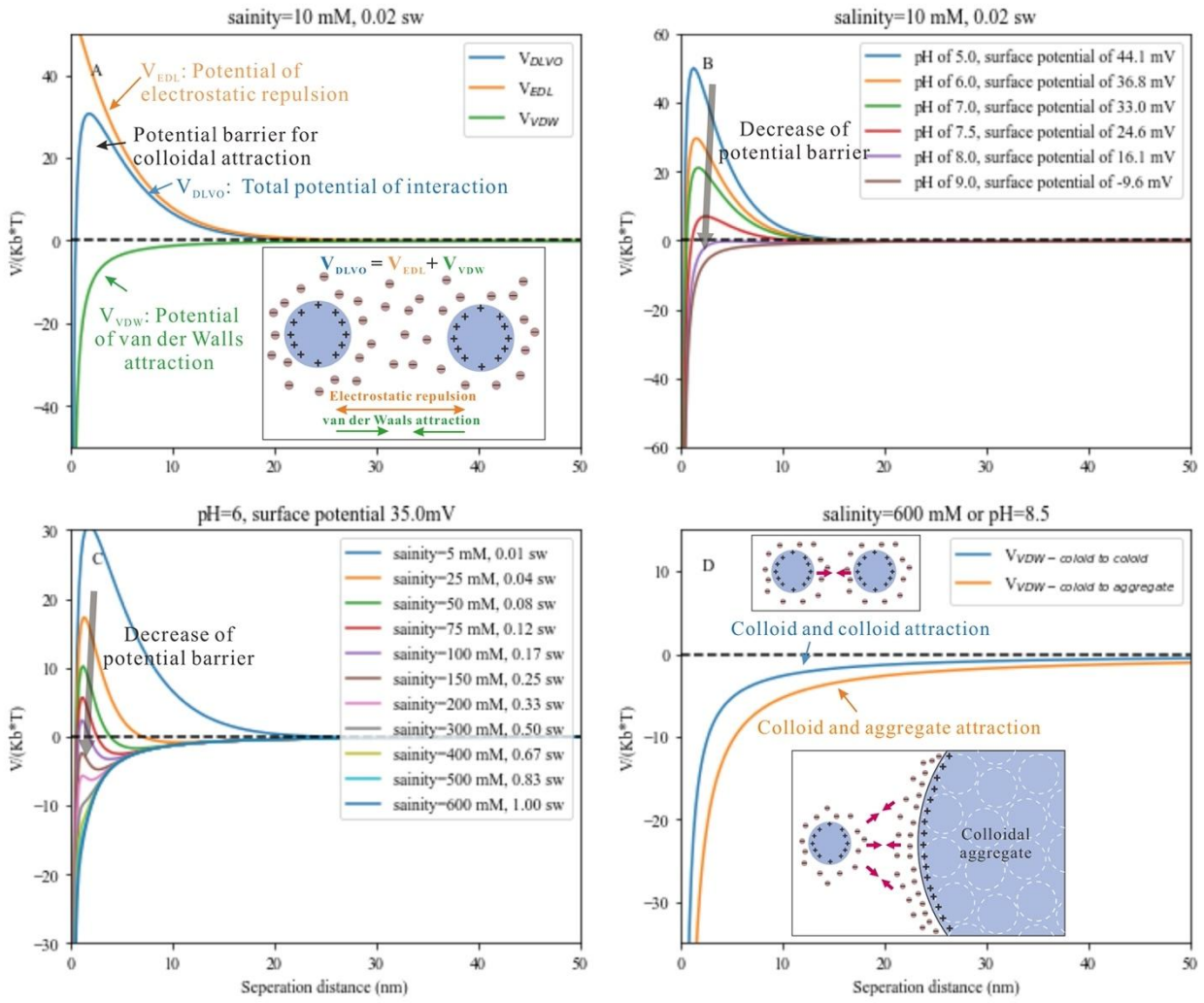


Fig. 3 EPMA and FIB–TEM analysis of stromatolitic ironstones. (A) to (C) Microscopy and EPMA mapping (Fe and Al) of stromatolitic ironstones with clay-rich laminae and hematite-rich laminates. (D) to (F) HAADF images and EDS mapping of clay-rich laminae showing edge–plate contacts among aggregates of platy hematite particles. (G) to (I) HAADF images and EDS mapping of hematite-rich laminae showing plate–plate contacts among aggregates of platy hematite particles. (J) High-magnification HAADF images showing details of hematein-illite aggregates. (K) and (L) High resolution HAADF images of hematite and illite show lattice d-spacings.



51

52 Fig. 4 Interaction potentials between Fe(III) oxyhydroxide particles calculated using DLVO
53 theory. (A) Interaction energies of V_{EDL}, V_{VDW}, and total interaction energy ($V_{Tot} = V_{EDL} + V_{VDW}$)
54 as functions of surface-to-surface distance in 10 mM NaCl solution. (B) Effect of pH at 10 mM
55 NaCl on total interaction energy (V_{Tot}) between Fe(III)-oxyhydroxide colloids. (C) Effect of NaCl
56 concentration at pH 6 on total interaction energy (V_{Tot}) between Fe(III)-oxyhydroxide colloids.
57 (D) Comparison of V_{VDW} between sphere–sphere and sphere–plate models in high-salinity solution
58 (600 mM NaCl, pH 8.5), where V_{EDL} approaches zero.

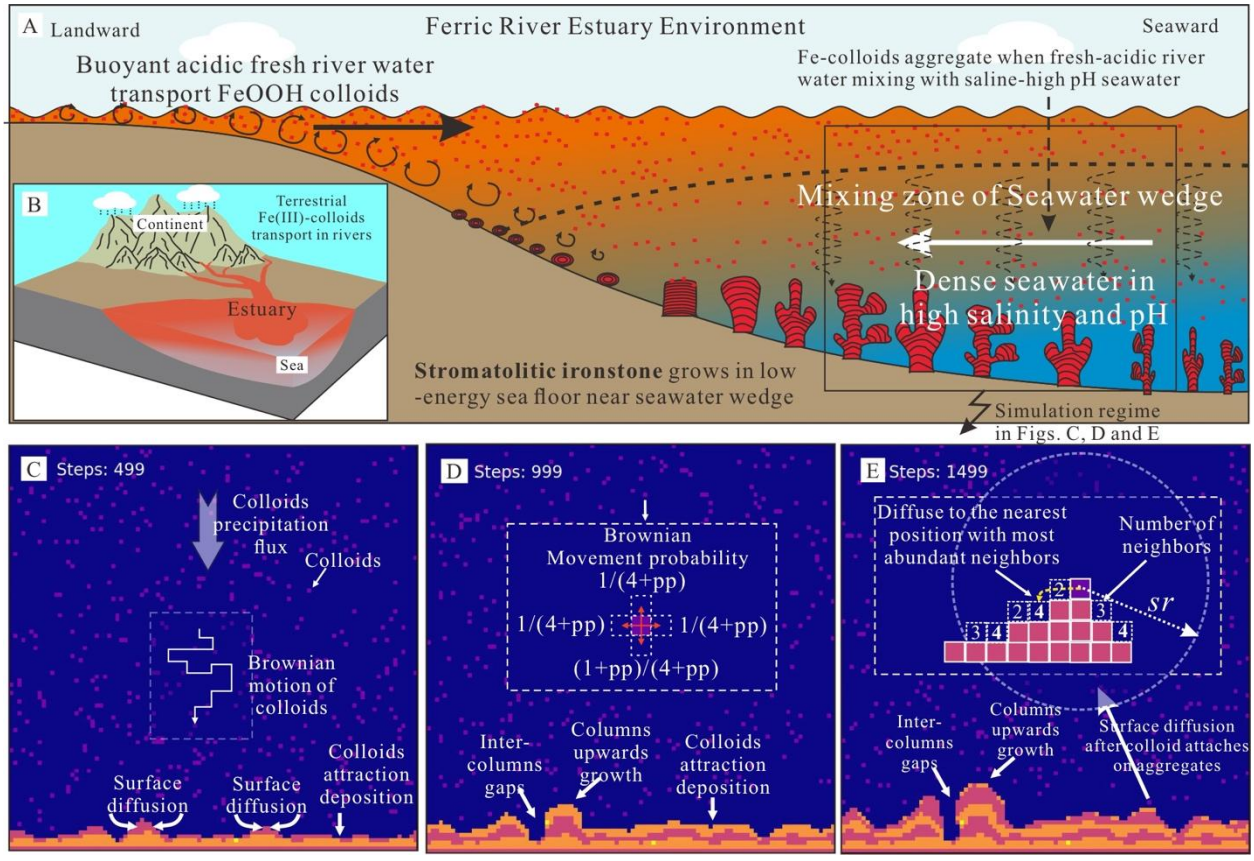


Fig. 5 Conceptual genetic model for ironstone formation in estuary and schematic cartons for the DLA-SD simulation. (A) and (B)Terrestrially derived Fe(III)-oxyhydroxide colloids were transported to estuarine environments via river systems. Mixing between river water and seawater increased salinity and pH, triggering rapid flocculation and precipitation of Fe(III)-oxyhydroxide colloids and promoting ironstone mineralization. (C) to (E) Schematic cartons of DLA-SD in a two-dimensional lattice, which shows colloids moving as Brownian motions with different moving probabilities in four directions. Also show is the surface diffusion of colloids after attached on the active aggregate surface by choosing the nearest position with most abundant neighbors within the surface diffusion radius.

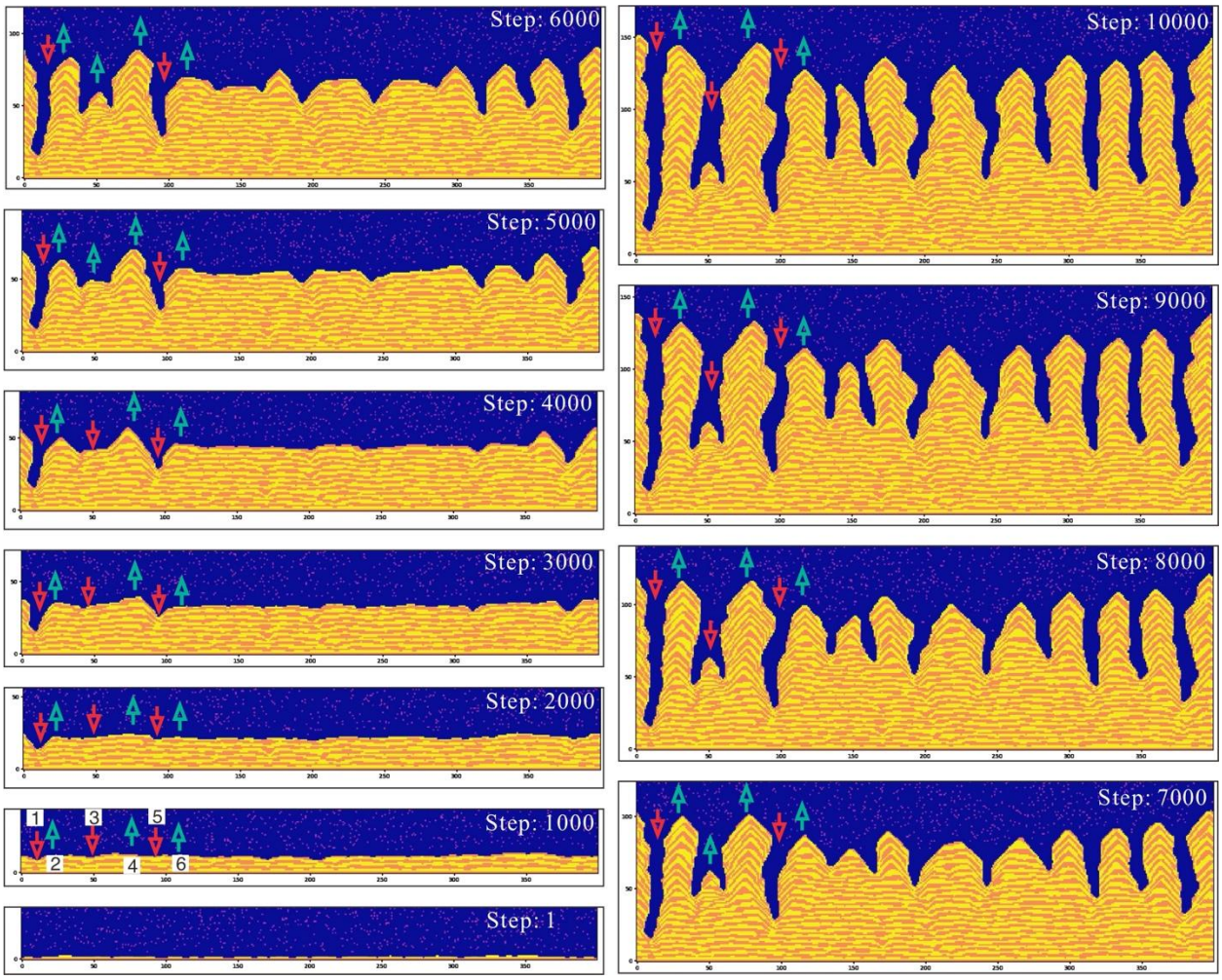


Fig. 6 Snapshots of simulation at different steps showing the emergence of stromatolitic structure on a flat substrate via two-way positive feedback of the DLA-SD mechanism, with blue and read arrows indicating the development of columns and depression, respectively.

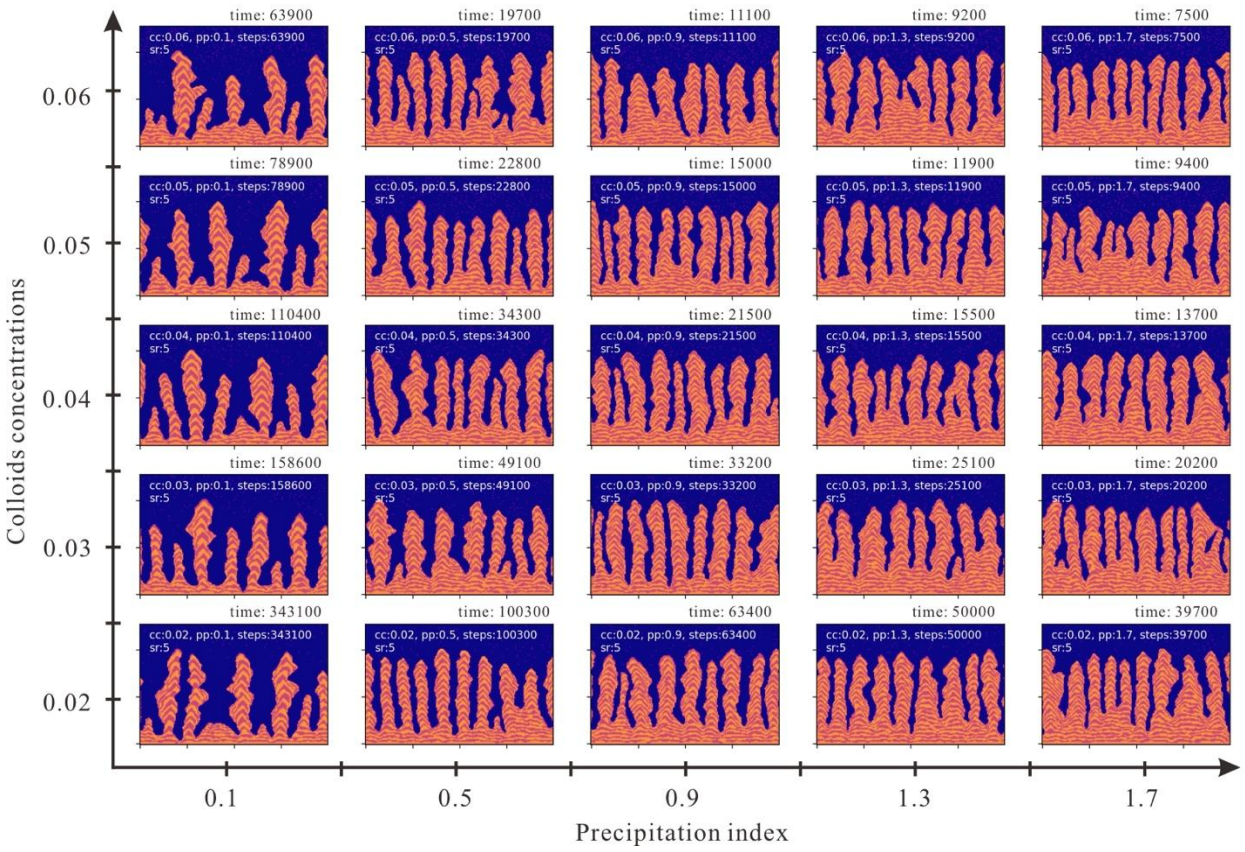


Fig. 7 DLA-SD simulation results showing influence of colloidal concentrations and movement indexes on the stromatolitic morphology. Results of a series of DLA-SD simulations with fixed surface diffusion radius ($sr = 5$) and variable colloidal concentration ($c = 0.02$, 0.03, 0.04, 0.05 and 0.06) and movement indexes ($pp = 0.1$, 0.5, 0.9, 1.3 and 1.7). The snapshots are simulation results when the highest column in each simulation reaches height of 200, and also shown are the time steps used for the growth.

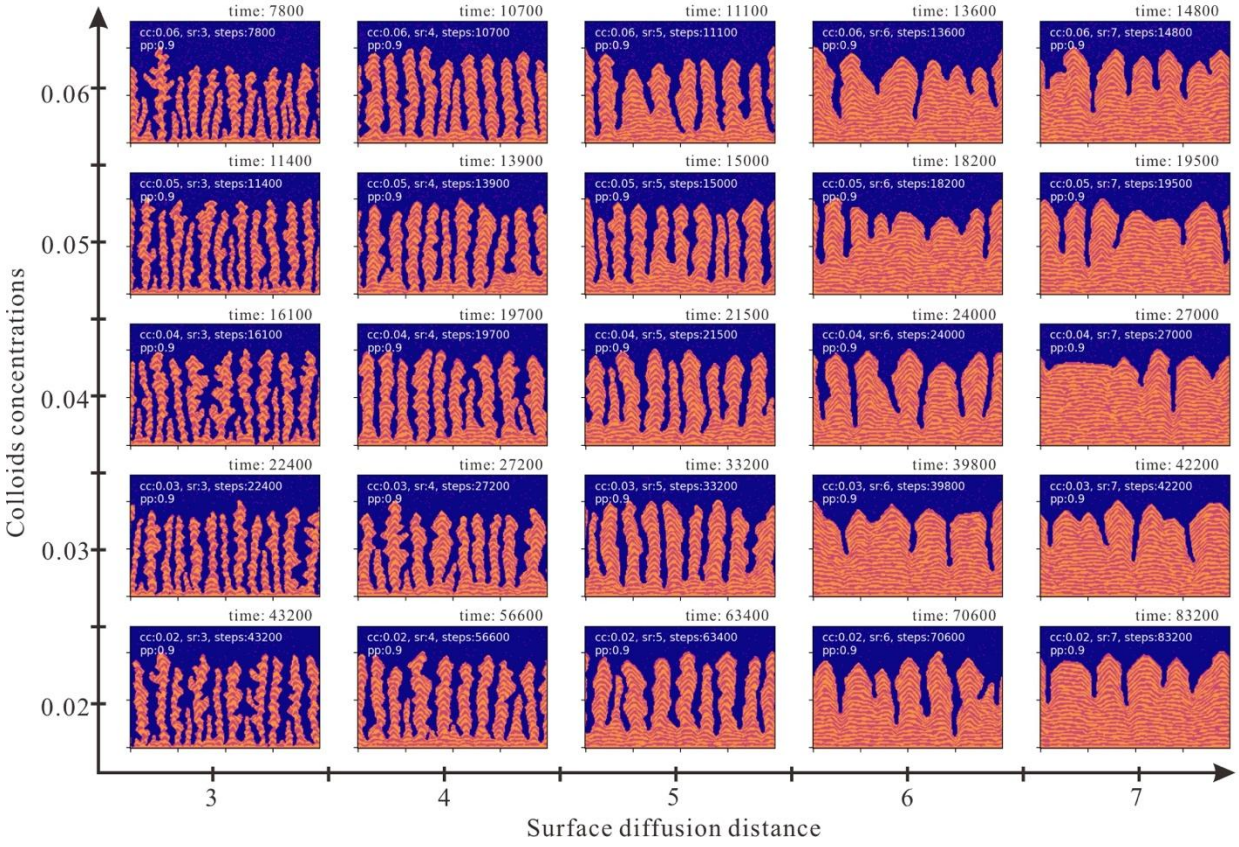


Fig. 8 DLA-SD simulation results showing influence of colloidal concentrations and surface diffusion radius on the stromatolitic morphology. Results of a series of DLA-SD simulations with fixed movement indexes (pp = 0.9) and variable colloidal concentration (c = 0.02, 0.03, 0.04, 0.05 and 0.06) and surface diffusion radius (sr = 3, 4, 5, 6 and 7). The snapshots are simulation results when the highest column in each simulation reaches height of 200, and also shown are the time steps used for the growth.

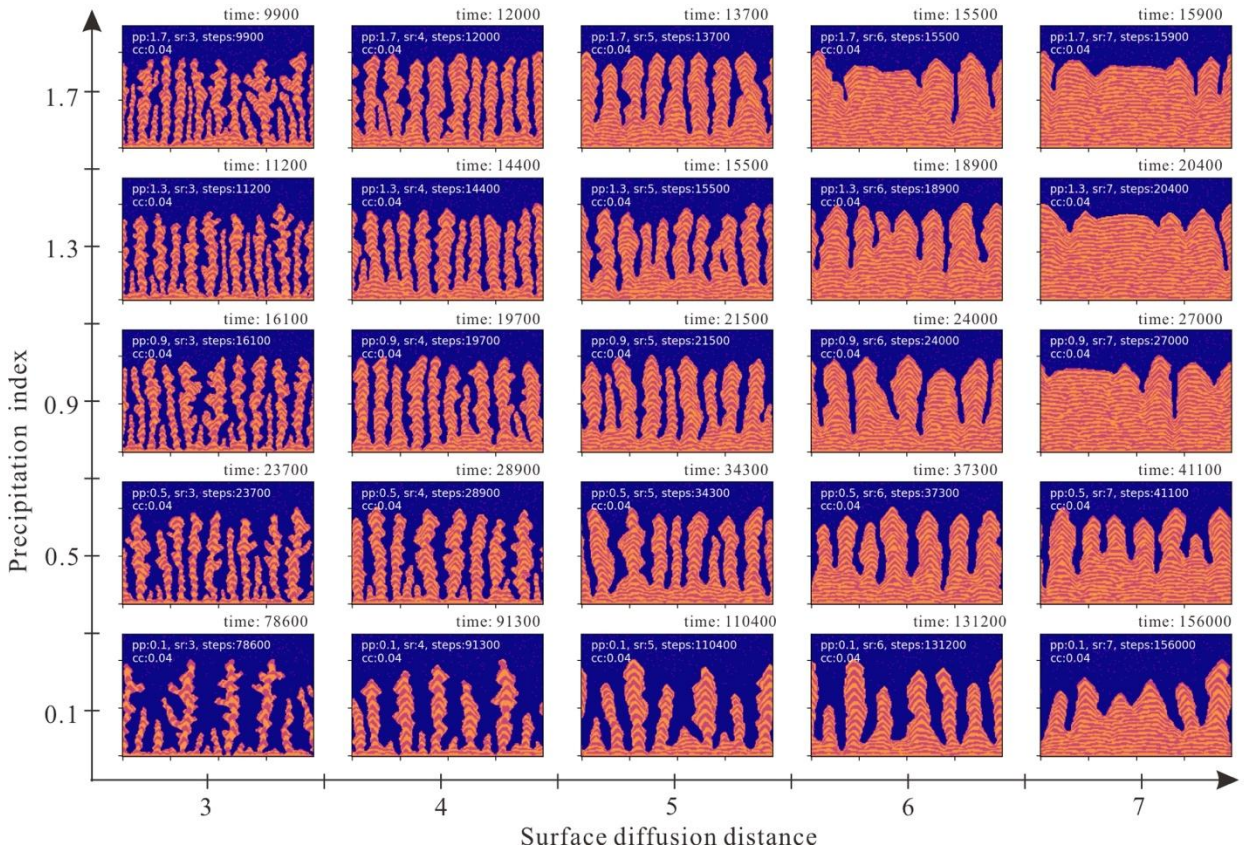


Fig. 9 DLA-SD simulation results showing influence of movement indexes and surface diffusion radius on the stromatolitic morphology. Results of a series of DLA-SD simulations with fixed colloidal concentration (c = 0.04) and variable movement indexes (pp = 0.1, 0.5, 0.9, 1.3 and 1.7) and surface diffusion radius (sr = 3, 4, 5, 6 and 7). The snapshots are simulation results when the highest column in each simulation reaches height of 200, and also shown are the time steps used for the growth.

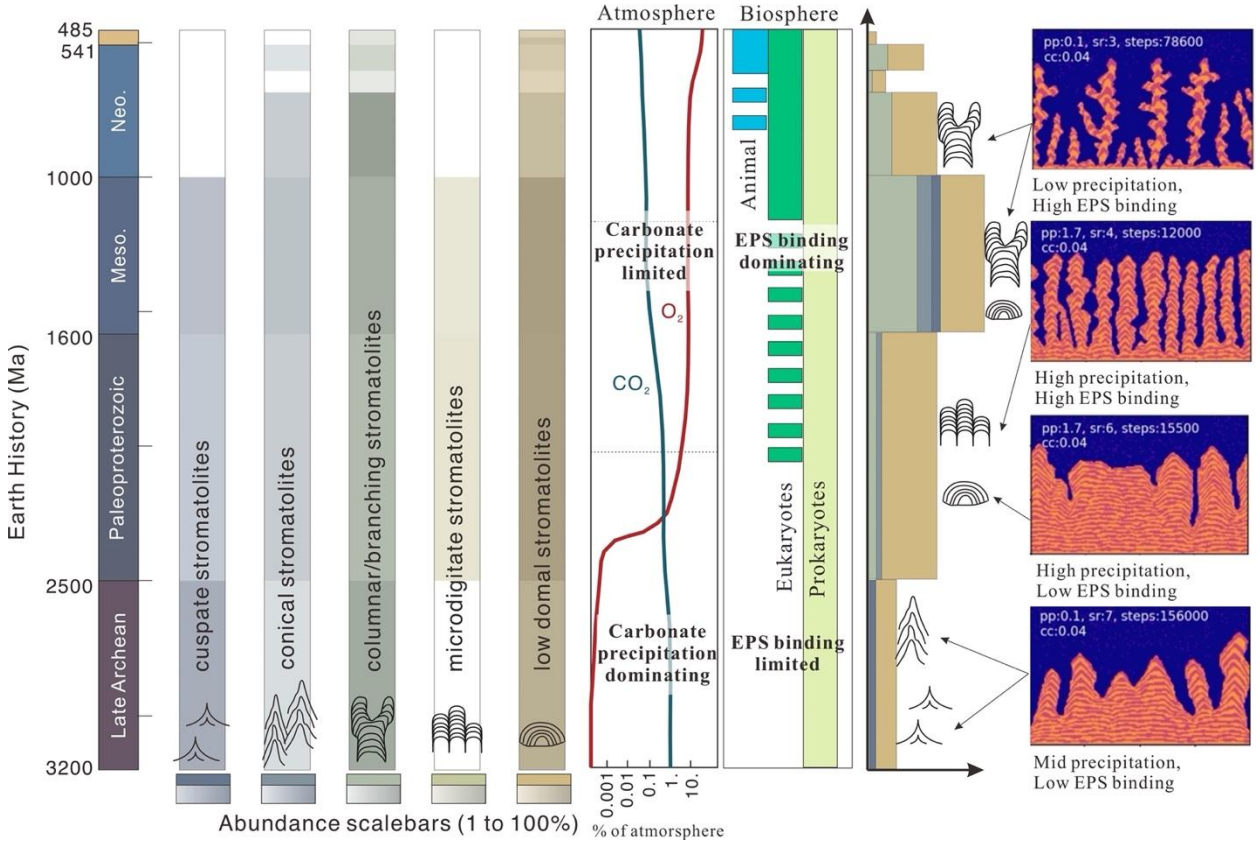


Fig. 10 Trends in the character and abundance of stromatolites, the variation of atmospheric O_2 and CO_2 pressures and the evolution of biosphere through Earth history. Changes in the abundance and morphology of stromatolites correspond to changes in saturation states of carbonate particles and the rise of eukaryotic communities that correspond to the precipitation index and surface diffusion radius of carbonate nano-particles. Trends in the character and abundance of stromatolites are modified from Cantine et al., 2020 [61]

Supplementary Files

This is a list of supplementary files associated with this preprint. Click to download.

- MovieS2DLAcc2pp2sr2.mp4
- Supplementarymaterialsstromatoliteironstonev7.pdf
- MovieS5DLAcc2pp0sr4.mp4
- MovieS4DLAcc2pp4sr0.mp4
- MovieS3DLAcc2pp4sr4.mp4
- MovieS1DLAcc2pp0sr0.mp4